Investigating the thermal decomposition of BP into B12P2: experimental insights and kinetic modelling at high temperatures

Yves Tahan, Olivier Rapaud, Nicolas Pradeilles, Pierre Carles, Alexandre Maître, Sarah Dine, Dominique Vrel, Hicham Moutaabbid, Yann Le Godec, Cécile Genevois, et al.

Acta Materialia 283 (2025) 120495

Contents lists available at ScienceDirect

Acta Materialia

journal homepage: www.elsevier.com/locate/actamat

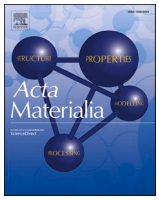

Investigating the thermal decomposition of BP into $B_{12}P_2$: experimental insights and kinetic modelling at high temperatures

Yves Tahan [a], Olivier Rapaud [a], Nicolas Pradeilles [a], Pierre Carles [a], Alexandre Maître [a,*], Sarah Dine [b], Dominique Vrel [b], Hicham Moutaabbid [c], Yann Le Godec [c], Cécile Genevois [d], Mathieu Allix [d]

[a] IRCER, UMR 731 CNRS, Centre Européen de la Céramique (CEC), 12 Rue Atlantis, 87068, Limoges Cedex, France
[b] LSPM, Sorbonne Paris Nord, 13, UPR 3407 CNRS, 99 avenue J.-B. Clément, Villetaneuse, 93430, France
[c] IMPMC, Sorbonne Université, UMR CNRS 7590, Muséum National d'Histoire Naturelle, 4 Place Jussieu, 75005, Paris, France
[d] CEMHTI, Univ. Orléans, UPR3079 CNRS, 1D avenue de la Recherche Scientifique, 45071 Orléans Cedex 2, France

ARTICLE INFO

Keywords:
Boron phosphide
Thermal decomposition
Kinetic modelling
Nucleation-growth mechanism

ABSTRACT

This study investigates the thermal decomposition of BP into $B_{12}P_2$, with a particular focus on the heterogeneous solid-gas mechanism involving BP powders synthesized via self-propagating high temperature reactions. Various techniques, including XRD, TGA, SEM, TEM, EELS and SAED, were combined to examine morphological and structural changes at different temperatures. The results reveal an ignition temperature for decomposition at 1120 °C, beyond which BP grains undergo fragmentation into smaller particles, accompanied by the release of phosphorous gases ($P_{2(g)}$, $P_{4(g)}$). Additionally, Rietveld refinements on thermally treated powders facilitated the determination of advancement rate values of the decomposition reaction under different isothermal conditions. Based on these kinetic data obtained at 1300 °C, a one-process nucleation-growth model with instantaneous nucleation and anisotropic growth has be established. In particular, the law, which describes the process for a spherical grain with inward development and a reaction occurring at the internal interface as the step determining the rate, displayed a strong correlation coefficient, offering novel insights into the kinetic evolution of the BP to $B_{12}P_2$ conversion. These results contribute to a deeper understanding of the thermal decomposition process and its underlying elementary mechanisms.

1. Introduction

Boron phosphide (BP) and boron sub-phosphide ($B_{12}P_2$) are semiconductors belonging to the III-V group having a wide indirect band gap (BP ≈ 2.1 eV [1–4], $B_{12}P_2$ ≈ 3.3 eV [5]), with exceptional properties such as high thermal conductivity (> 400 $W.m^{-1}.K^{-1}$ at room temperature) [6–9], and remarkable mechanical properties including high hardness (BP: Hv ≈ 30–38 GPa [1,10–12], $B_{12}P_2$: Hv ≈ 35–37 GPa [10, 12–14]), Young's modulus (> 360 GPa), bulk modulus (> 170 GPa), shear modulus (> 150 GPa) and a very low density (BP: 2.9 $g.cm^{-3}$, $B_{12}P_2$: 2.5 $g.cm^{-3}$) [10]. Due to their outstanding features, these materials are considered as excellent candidates for various structural applications. Despite the growing interest in the potential applications of BP and $B_{12}P_2$, there has been limited research into their properties and characterizations.

The literature highlights several potential applications for BP, particularly in semiconductor devices, including its use as an anode material for alkali metal-based batteries [15] or as a layer for LEDs and laser diodes [16]. Despite its unique properties, BP has not gained widespread industrial use. Historically, one of the main challenges in studying BP was its difficult synthesis due to its high melting point [17–19], the release of gaseous phosphorus and decomposition at high temperatures [1,20–24]. Consequently, BP synthesis was complex, costly and had a low yield.

Recently, there has been a renewed interest in BP, particularly in the measurement of thermal conductivity on single crystals [1,8,9], and research on p- or n-type BP samples [25–29]. Additionally, the deployment over the last few decades of original methods for boron phosphides, such as Self-propagating High-temperature Synthesis (SHS) and mechanochemistry [13,30–33], has enabled the production of BP

* Corresponding author.
E-mail address: alexandre.maitre@unilim.fr (A. Maître).

https://doi.org/10.1016/j.actamat.2024.120495
Received 12 April 2024; Received in revised form 24 September 2024; Accepted 19 October 2024
Available online 24 October 2024

powders in large quantities, even on an industrial scale. Whether through SHS or mechanochemistry, the final product consistently contains a primary BP phase with a content exceeding 97 %, alongside a secondary phase of $B_{12}P_2$ [32,33].

Concerning the crystallographic structure, BP exhibits a zinc blende structure with a $F\bar{4}3m$ space group and a lattice parameter a = 4.538 Å [34]. Boron atoms occupy half of the tetrahedral sites. The zinc blende structure, or sphalerite structure, is commonly found in III-V semiconductors such as cubic boron nitride, cubic boron arsenide or gallium phosphide. $B_{12}P_2$ has a rhombohedral crystal structure with a $R\bar{3}m$ space group and lattice parameters a = 5.985 Å and c = 11.842 Å [23,35]. The structure consists of B_{12} icosahedra linked together by P-P lateral chains to form a three-dimensional framework.

Following the discovery of BP in 1891 by Moissan [36,37] and Besson [38], the first synthesized BP powder was subjected to temperatures exceeding 1000 °C in a hydrogen-reducing atmosphere [36,37,39]. After several hours of exposure, thermal decomposition occurred, leading to a less phosphorus-rich state with a proportionate release of phosphorus gas. This new phase demonstrated greater thermal stability. Since the thermal decomposition of BP is not complete, the product appears to be composed of a mixture of the two phosphides.

To identify the less phosphorus-rich compound Williams et al. in 1959 heated BP powder above 1100 °C under a reduced pressure of <150 Pa, leading to a light grey residue [21]. Through thermogravimetric analyses and chemical methods, this phase was identified as $B_{12}P_2$. It was proposed that BP decomposes into $B_{12}P_2$ with the release of $P_{2(g)}$.In 1963, Perret et al. estimated the decomposition temperature to be around 1180 °C at normal pressure (1 atm) by conducting heat treatments at different temperatures and analysing the composition through chemical analysis [20]. After a 1-hour heat treatment at 1180 °C and 1250 °C, a mixture of BP and $B_{12}P_2$ phases were obtained. At 1500 °C and higher, the decomposition was complete after 1 hour, yielding only $B_{12}P_2$. Several studies have reported that the thermal decomposition of BP into the $B_{12}P_2$ phase occurs around 1150 °C in a reducing atmosphere or under vacuum [1,20–22,24,40]. To clearly establish the decomposition reaction, Alikhanyan et al. conducted a mass spectrometric investigation of the vaporization of BP in 1975 [22]. They identified the volatile phosphorus species during decomposition as $P_{4(g)}$ and $P_{2(g)}$ and proposed several hypotheses for the decomposition of BP.

Although experimental data are currently available in the literature concerning the decomposition temperature, the nature of phase formed, the associated mechanism decomposition remain poorly understood, particularly with respect to (micro)structural evolution. While it is known that temperature affects the BP decomposition, the kinetics of this process have not been thoroughly investigated.

This gap in understanding is particularly significant given the excellent mechanical properties and the increasing production of BP and $B_{12}P_2$ through SHS or mechanochemistry.

Such an understanding of the mechanism underlying the thermal decomposition of the BP phase could have a positive impact in the synthesis and sintering ability of BP or $B_{12}P_2$ micro- or nanopowders. In particular, the determination of the thermal decomposition kinetics and knowledge of the limiting step are crucial in order to identify the appropriate experimental conditions for the synthesis (by high-energy ball milling or by SHS route) of pure, fine, regularly shaped or even equiaxed BP or $B_{12}P_2$ powders. If $B_{12}P_2$ nanopowders are to be synthesized, the early stages of crystal nucleation and growth need to be thoroughly investigated to avoid exaggerated growth and coalescence of these particles.

Finally, it is well known in the literature that gas release during sintering can induce the formation of residual porosities in more or less large volume fraction. Thus, the partial thermal decomposition of the BP phase during sintering can induce the formation of residual porosities that may be difficult to remove, as well as possible expansion of the specimens.

A good understanding of the reaction mechanism involved in the thermal destabilization of boron phosphide (BP) is a major issue to control the characteristics of the obtained $B_{12}P_2$ powders, mainly their grainsize and chemical composition. A rigorous control of the mesh parameters is mandatory for subsequent study of the elementary processes arising during further sintering, shaping or other ceramic processing.

This works reconsiders the reaction mechanism involved in the thermal destabilization of boron phosphide (BP) by coupling TEM, electron microdiffraction, EELS analyses of powders taken at various advancement steps of the thermal decomposition. This structural approach allows to discuss the mechanisms by which the products are destabilized to identify the nucleation and growth mechanisms involved in the $B_{12}P_2$ formation.

2. Materials and methods

2.1. Characterisation methods

To identify the crystalline phases, X-ray diffraction analyses of raw powders have been performed using a Bruker D8 Advance A25 diffractometer with a Cu $K_{\alpha1,2}$ source ($\lambda CuK_{\alpha1}$ = 1.5406 Å, $\lambda Cu_{K\alpha2}$ = 1.54439 Å). A linear XE-T detector is used to avoid the use of a K_β Ni filter. The diffractometer involves a Bragg-Brentano θ-θ geometry and the divergence slit is fixed over a 20–90° angular range. The time per step and the step size were fixed at 0.7 s and 0.014° respectively. BP and $B_{12}P_2$ XRD data should be retrieved in the Powder Diffraction File™ (PDF®) with the following corresponding references: PDF: 011–0119 for BP and PDF: 048–1166 for $B_{12}P_2$. The morphological features of particles were studied using Scanning Electron Microscopy (SEM) (Quanta 450 FEG, FEI) and Transmission Electron Microscopy (TEM) (JEM-2100F, JEOL). TEM was used to obtain Selected-Area Electron Diffraction (SAED) patterns for crystal structure identification. Chemical information was obtained by high angle annular dark field – scanning transmission electron microscopy (HAADF-STEM) imaging and electron energy loss spectroscopy (EELS), using a 0.13 nm spot size. The acquisitions were carried out with a JEOL JEM-ARM200F Cold FEG transmission electron microscope operating at 200 kV, equipped with a double spherical aberration corrector and fitted with a Gatan GIF (Gatan Imaging Filter). EELS data, spectrum-imaging and punctual analyses, were acquired with a dispersion of 0.1eV/channel and in DUAL-EELS mode in order to realign the spectra based on the zero-loss peak, to subtract the background and to remove plural scattering effects a posteriori. EELS reference spectra were collected using well-crystallized grains of BP (Figure S1) and $B_{12}P_2$ (Figure S2). Sample preparation consisted of homogeneously dispersing fine sample powder in ethanol, then depositing one droplet of this suspension onto a TEM amorphous holey carbon-coated copper grid and left to dry. Thermogravimetric analyses (TGA) under flowing argon, with a heating rate of 20 °C/min were carried out using a STA 449 F3 apparatus from Netzsch, Germany, to investigate the thermal stability and identify the temperature decomposition of the BP phase. The apparatus was equipped with an Al_2O_3 TGA-DTA sensor including type S Pt-PtRh10 % thermocouples, Al_2O_3 crucibles and a SiC furnace.

2.2. Synthesis methods and thermal treatments

BP powders were only produced by Self-propagating High temperature Synthesis (SHS) based on the reduction of BPO_4 amorphous boron phosphate (produced by the method described in [41]) with magnesium metal (Eq (1)) and was described by Mukhanov et al. [30]. The overall equation followed during this synthesis is given below:

$$BPO_4 + 4Mg \rightarrow BP + 4MgO \quad (1)$$

This powder was characterised by X-ray diffraction and showed almost a single phase (Fig. 1). During the synthesis, the local

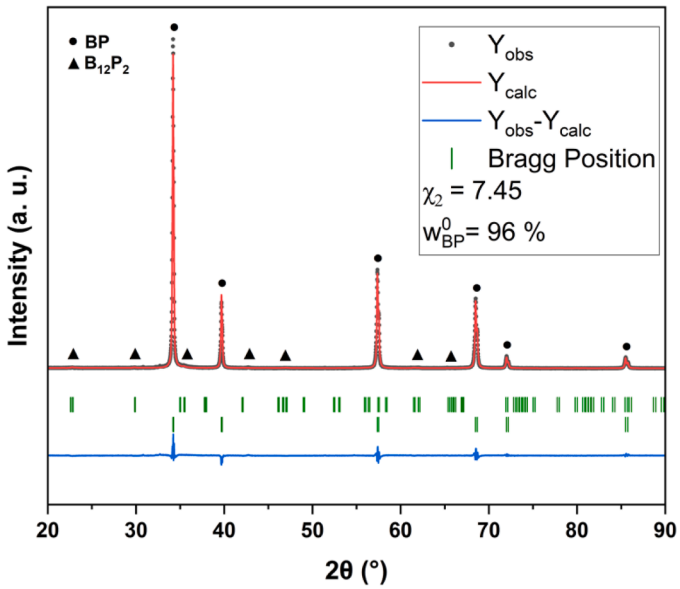

Fig. 1. X-ray diffraction (XRD) pattern of the initial BP powder produced by SHS and its Rietveld refinement.

temperature can reach the temperature of the decomposition of BP at which occurs the formation of the $B_{12}P_2$ secondary phase [30].

Thermal treatments on SHS-synthesised BP powder were performed with a Nabertherm VHT 8/22-GR graphite furnace under dynamic vacuum. A heating rate of 10 °C/min was applied followed by a defined dwell time. The holding temperature ranged between 1100 °C and 1300 °C in order to determine the thermal stability range.

2.3. Rietveld refinement: description of the fractional conversion

In order to follow the reaction advancement of the decomposition, a fractional conversion of the decomposition (α) was proposed (Eq (2)), considering the weight loss of the BP phase after a thermal treatment:

$$\alpha = \frac{w^0_{BP} - w^t_{BP}}{w^0_{BP}} \quad (2)$$

To determine the weight loss, Rietveld refinements were applied to the XRD patterns using the Fullprof software to calculate the mass fraction of BP and $B_{12}P_2$ phases, respectively. In the Eq. (2), w^t_{BP} is the mass fraction of the BP obtained after thermal treatment and w^0_{BP} is the mass fraction of BP before thermal treatment, thus corresponding to the mass fraction of BP in the initial powder. Rietveld refinement was performed on the initial BP powder leading to $w^o_{BP} = 96\%$ (see Fig. 1).

3. Experimental results

3.1. Morphological and structural characterizations of the starting BP powder

To analyse the size and morphology of the starting BP powder, TEM and SEM techniques were combined. On the basis of SAED, TEM and SEM images, two sets of boron phosphide (BP) particles can be distinguished: i) the first group showed faceted grains ranging in size from 100 nm to 1 μm; ii) the second group consisted of grains sized between 10 and 50 nm (Fig. 2). Through SEM image analysis, the average grain size was estimated to be 306 nm from measurements of 350 grains.

The TEM images in Fig. 3 illustrate the appearance of $B_{12}P_2$ grains on the surface of BP grains. This presence can be attributed to the decomposition of BP resulting from high local temperatures during SHS synthesis. Since it is impossible to observe continuity of the crystal lattice

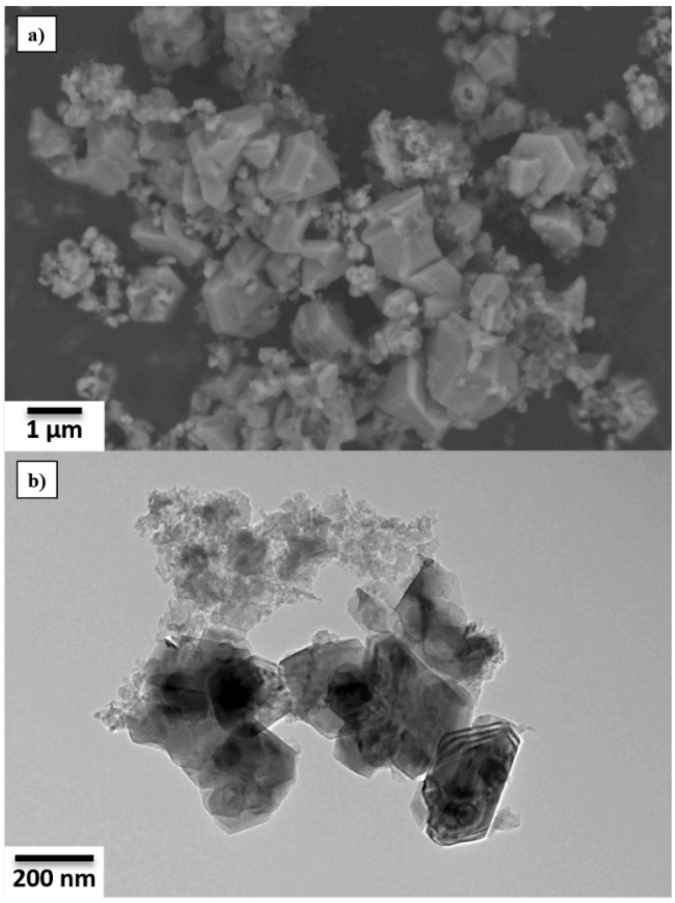

Fig. 2. Scanning electron microscopy (a) and transmission electron microscopy (b) images of the initial boron phosphide (BP) powder synthesised by SHS.

and, therefore, simple relationships between the main crystallographic axes of the original phase (BP) and the produced phase ($B_{12}P_2$), it can be deduced that there is no topotactic relationship between them.

3.2. Thermal treatment

3.2.1. Identification of the decomposition temperature by TGA/DTA

To determine the decomposition temperature of BP into $B_{12}P_2$, a thermogravimetric analysis was conducted using TGA/DTA up to 1500 °C (Fig. 4). At lower temperatures, around 620 °C, a minor weight loss of approximately 1.3 % was observed, likely attributed to the dissociation of surface-adsorbed gases [1]. At higher temperatures, a more substantial weight loss of approximately 50 % was identified. This weight loss can be interpreted as the thermal decomposition of the BP phase into $B_{12}P_2$ associated with a phosphate gas outflow which initiated at approximately 1120 °C. Nevertheless, the gas produced during this latter reaction notably damaged the device, particularly the platinum thermocouple.

3.2.2. Study of the early stages of the thermal decomposition

Structural and morphological analyses were performed on BP powders subjected to a 1-hour thermal treatment, aiming to investigate the early stages of decomposition. Following treatment at 1100 °C for 1 hour, no significant change in fractional conversion was observed, indicating that decomposition had not yet initiated. However, the XRD patterns in Fig. 5 revealed the emergence of the $B_{12}P_2$ phase for temperatures exceeding 1150 °C. In the temperature range of 1150–1250 °C, SEM and TEM images (Fig. 6) depicted various morphological transformations in the initially faceted BP grains.

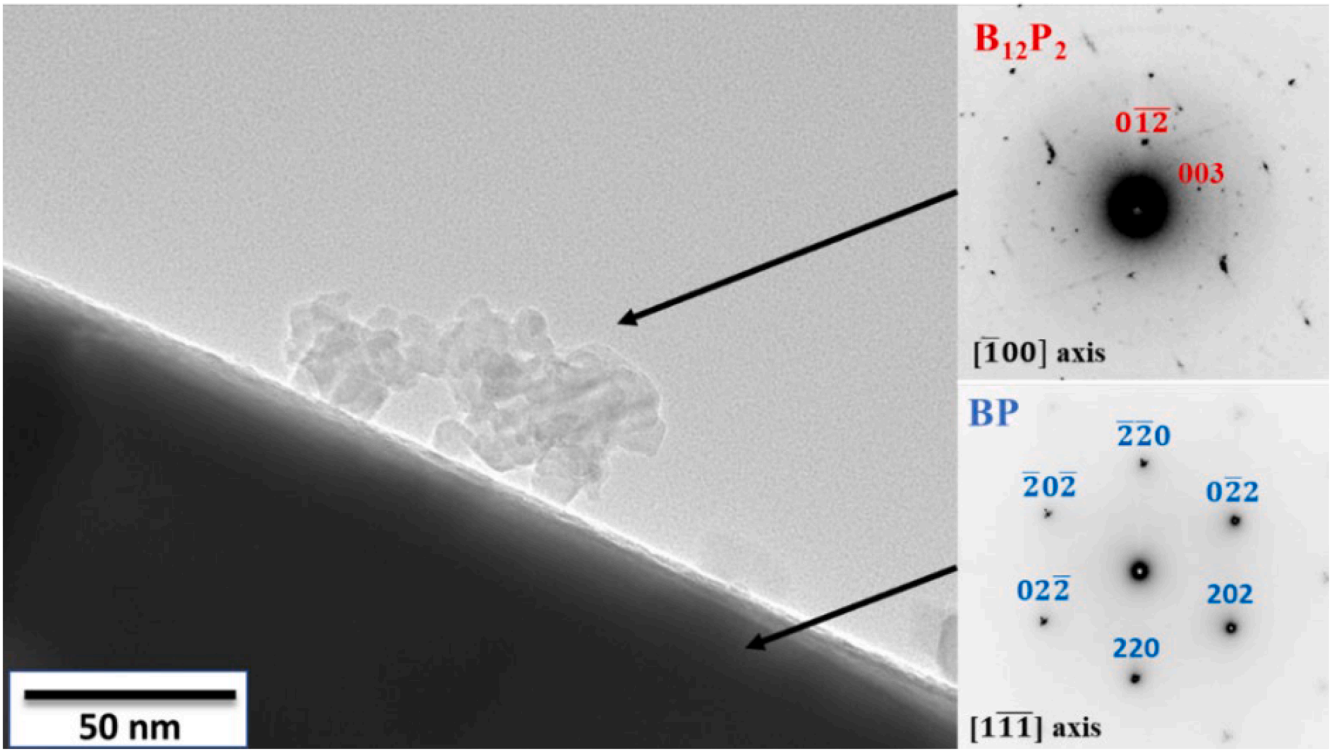

Fig. 3. Transmission electron microscopy images of the surface of a faceted BP grain. $B_{12}P_2$ polycrystalline grains were identified using SAED patterns (right side).

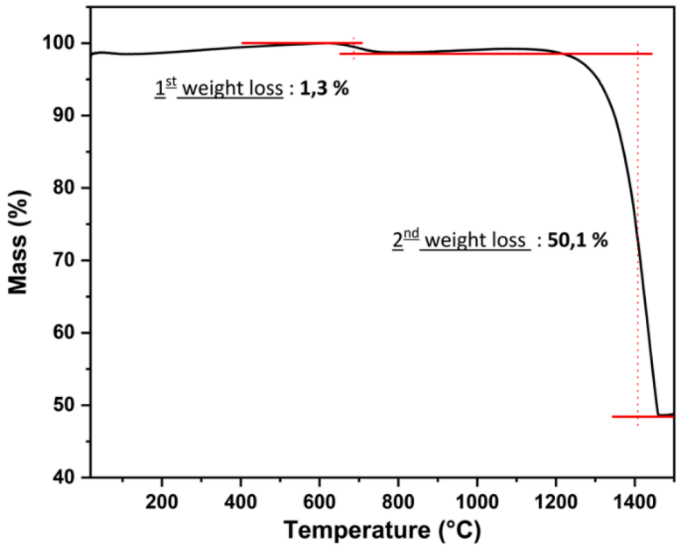

Fig. 4. TGA analysis of a SHS-synthesised BP powder.

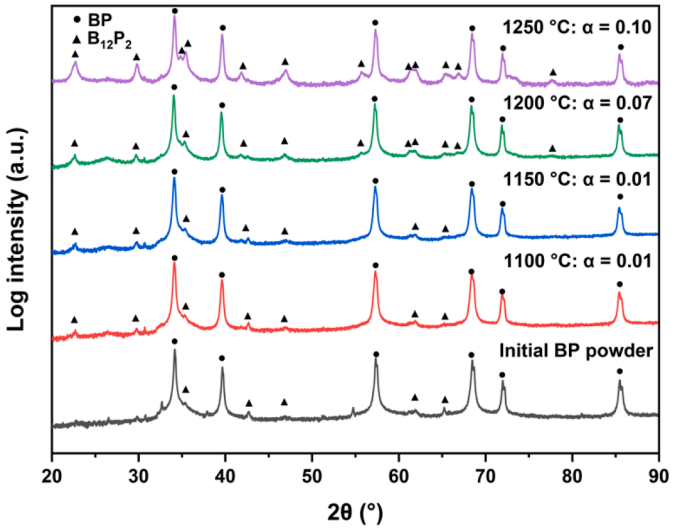

Fig. 5. X-ray diffraction (XRD) patterns of the initial BP powder compared to those subjected to different thermal treatments during 1 h, with a log intensity scale to reveal the secondary phases.

Under 1100 °C, no morphological changes have been observed (Figure S3). These faceted grains were identified as BP crystallites through the indexation of the SAED pattern of the grain surface (Fig. 6c). When the temperature exceeded the decomposition threshold (>1120 °C), a 1-hour heat treatment at 1150 °C initiated the fragmentation of faceted grains into smaller ones. Upon deeper examination of SEM images depicting the powder subjected to 1150 °C (Fig. 6d), it became apparent that not all grains displayed fragmented surfaces. Furthermore, these grains retained their original shape, as observed in the initial powder (Fig. 6a and Fig. 6b). Additionally, cavities were observed on the surface of the grains, favoured at higher temperature, for example at 1200 °C (Fig. 6f). It is likely that these cavities result from the formation of volatile products, in particular from the release of phosphorus gas. The origin of these cavities will be further explained in the discussion section.

Therefore, this fragmentation phenomenon favors the emergence of additional small grains, which would ulimatively lead to a reduction in the average grain size. This can be observed when comparing the morphology of the grains in Fig. 6b with those in Fig. 6h. However, it is difficult to deduce from the SEM images alone which phase, between BP or $B_{12}P_2$, is associated with each grain. To clearly identify the formation of $B_{12}P_2$, phase identification was performed using SAED patterns alongside the TEM images in Fig. 6a, c, e, and g.

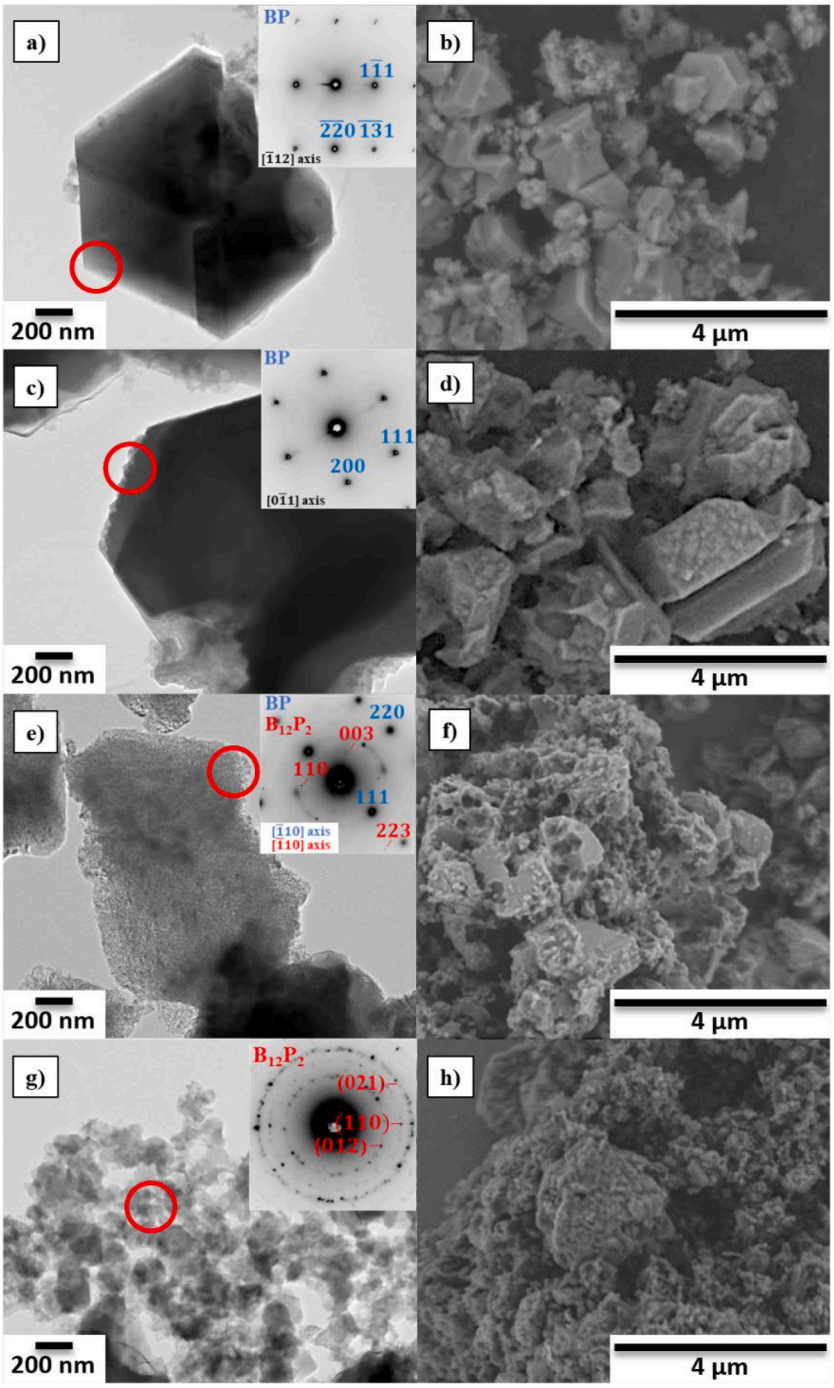

Fig. 6. TEM images on the left and SEM images on the right of BP powders subjected to different thermal treatments. SAED patterns were obtained from the red areas in the images. (a) and (b) Initial powder, (c) and (d) 1150 °C for 1 hour, (e) and (f) 1200 °C for 1 hour, (g) and (h) 1250 °C for 1 hour.

When the temperature was raised to 1200 °C (with a 1-hour dwell time), fragmentation extended across the entire surface. Additionally, the SAED pattern in Fig. 6e confirmed the presence of both BP and $B_{12}P_2$ phases. In contrast to the powder treated with a 1-hour dwell time at 1150 °C, the heat treatment at 1200 °C resulted in the fragmentation of nearly all faceted grains, as illustrated in Fig. 6f. Considering that locally and simultaneously the grains of the BP phase undergo a fragmentation phenomenon and that the crystallites of the $B_{12}P_2$ product phase's germination and growth, distinguishing between them becomes challenging, even with TEM techniques.

To differentiate these phases, EELS spectroscopy coupled with HAADF-STEM imaging were performed on the surface of a region of grains undergoing fragmentation, as shown in Fig. 7. This combined technique allowed for a precise examination of atomic composition gradients on the surface of BP grains during decomposition. In the mapped region (Fig. 7a and b), three elements were identified: carbon (C-K edge at 282.5 eV), boron (B-K edge at 188 eV), and phosphorus (P-$L_{2,3}$ edge at 129 eV). The presence of carbon could be explained by minor contamination from the graphite. Topographically, the mapped area exhibits variations in relief, including cavities and thinner regions. The elemental mapping in Fig. 7b shows that the boron content remains constant, except in areas devoid of material, while the phosphorus concentration varies across the region. In one of the thinner regions, marked as Point 1, phosphorus is sparsely present. The EELS spectrum at

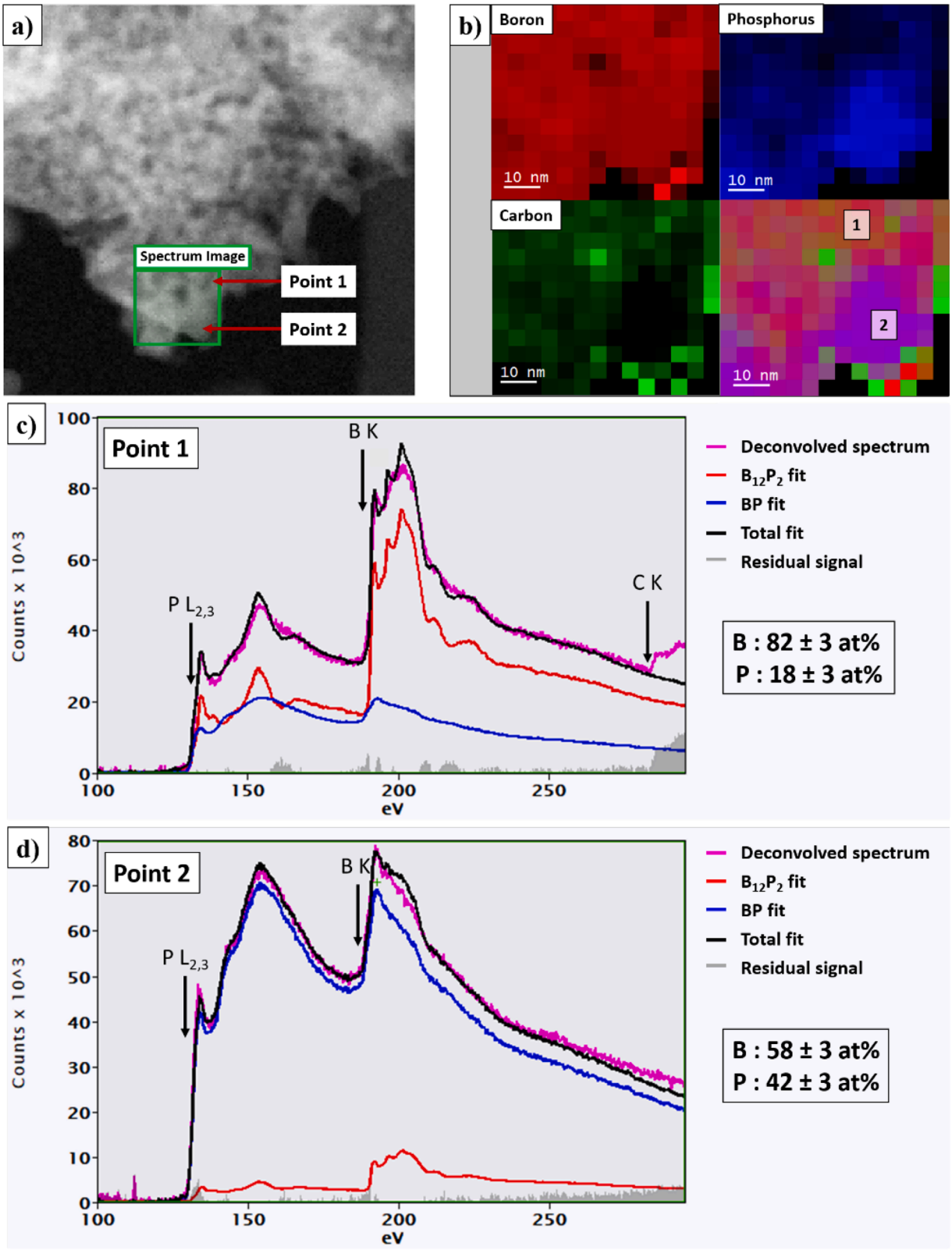

Fig. 7. (a) HAADF-STEM image of a fragmented BP grain after 4 hour at 1200 °C; (b) STEM-EELS elemental mapping (at %) of boron (K edge), phosphorus ($L_{2,3}$ edge), and carbon (K edge) for the same grain; (c) EELS spectrum at Point 1, and (d) EELS spectrum at Point 2.

Point 1 (Fig. 7c) estimates the atomic percentage of phosphorus at 12 ± 3 at%, with boron at 82 ± 3 at%, which broadly corresponds to the composition of $B_{12}P_2$ (14.3 at% P - 85.7 at% B). Near this area, at Point 2, a higher concentration of phosphorus is observed, with the EELS spectrum in Fig. 7d estimating the atomic percentage of phosphorus at 42 ± 3 at%, and boron at 58 ± 3 at%, indicating a composition slightly different from BP. By decomposing the spectra by MLLS (Multiple Linear Least Squares) fitting routine (methodology proposed in Supplementary

Information) using the reference spectra acquired for BP and $B_{12}P_2$ (Figures S1 and S2), small amounts of BP in the spectrum of point 1 and of $B_{12}P_2$ in the spectrum of point 2 are highlighted, explaining the small deviation found compared to the stoichiometric composition. An elemental composition gradient is thus clearly visible in this region, where the precipitation of the $B_{12}P_2$ phase appears to occur near a phosphorus-deficient, potentially sub-stoichiometric BP phase. At 1250 °C, with a 1-hour dwell time, isolated polycrystalline grains of $B_{12}P_2$ were observed and identified in Fig. 6g. The thermally treated powders exhibited a trend of decreasing grain size, starting at 1150 °C and accelerating with increasing temperature until all the faceted grains were fragmented. This trend was further supported by SEM and TEM observations, which showed a decrease in the number of faceted grains in favor of fragmented grains.

3.2.3. *The approach of nucleation-growth of $B_{12}P_2$ crystallites*

To gain a deeper understanding of the nucleation-growth process, TEM observations and SAED acquisitions were conducted on the surface of fragmented BP grains. In Fig. 8a and b, HAADF-STEM image and EELS spectrum-imaging acquisitions are presented showing the surface of an ongoing fragmented grain from a powder treated at 1200 °C during 1 h The phase mapping presented in Fig. 8b was obtained by decomposing the spectrum imaging acquired by MLLS (Multiple Linear Least Squares) fitting routine using the reference spectra (Figures S1, S2 and S4), showing the presence of 4 phases including BP, $B_{12}P_2$, carbon and hexagonal BN. The hexagonal BN observed results from minor cross-

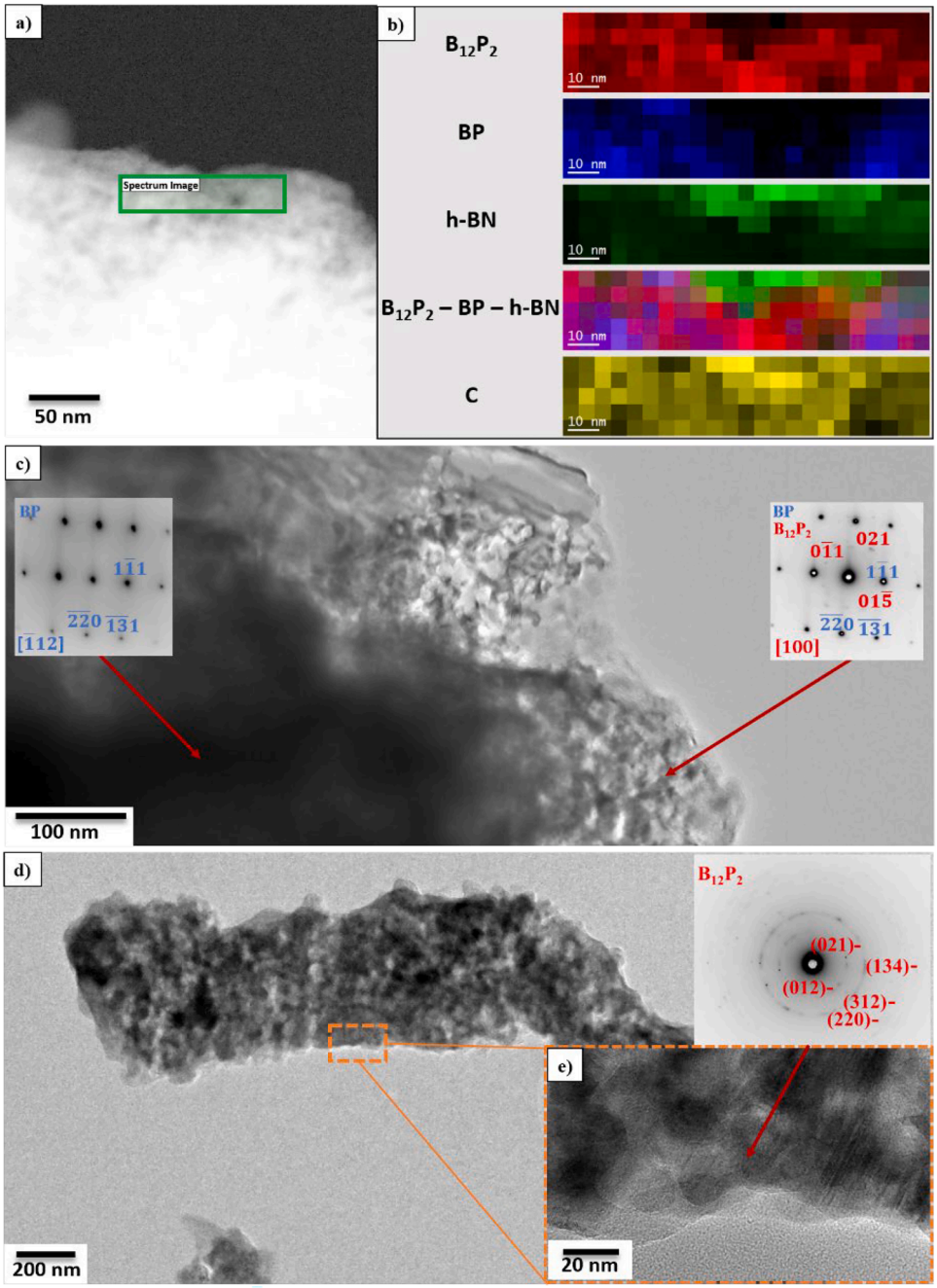

Fig. 8. TEM images, SAED patterns, HAADF-STEM images, and STEM-EELS mapping illustrating nucleation and growth stages: (a) and (b), Fragmented BP grains after 1 hour at 1200 °C; (c) TEM image of another BP grain treated under the same conditions; (d) and (e) $B_{12}P_2$ grains observed after 4 h at 1250 °C with (e) showing a specific zone outlined in orange in (d). (For interpretation of the references to colour in this figure legend, the reader is referred to the web version of this article.)

contamination in the furnace, where a few layers may have been deposited on the outermost surface. However, these filaments appear to be limited to the extreme surface and do not interfere with the phases under study. The $B_{12}P_2$ phase appears to be homogeneously distributed across the entire surface. The BP phase, on the other hand, has been identified in the thicker regions and coexists with the $B_{12}P_2$ phase. This analysis indicates that the nucleation/growth of the $B_{12}P_2$ phase occurs uniformly on the grain surfaces and progresses towards the thicker regions corresponding to BP. The separation of the two phases is located at the interface where the reaction occurs, which is characteristic of the onset of the growth phenomenon. Examining a different grain from the same sample (1200 °C – 1 h) in Fig. 8c, the thicker areas correspond to the BP phase, while the thinner, fragmented zones reveal the presence of both BP and $B_{12}P_2$ phases. By examining the fragmented zone, cavities can be observed throughout the area, probably due to the release of phosphorus gas in the form of $P_{2(g)}$ or $P_{4(g)}$.

To assist the formation and the growth of the $B_{12}P_2$ phase, heat treatments with longer dwell times were performed. By heat-treating the BP powder at 1250 °C for a 4-hour dwell time, the nucleation-growth of $B_{12}P_2$ was favoured, resulting in a fractional conversion $\alpha = 0.45$ (Fig. 8d and e). Fig. 8d shows an overview of a group of grains whose outline suggests the initial shape of a BP grain. Upon examining a more specific area (Fig. 8d), it is observed that this grain has been entirely divided into a multitude of smaller grains. A SAED pattern taken at the edge revealed that the observed grains, ranging in size from 20 to 50 nm, are exclusively $B_{12}P_2$. No trace of BP was detected, suggesting that the BP matrix has been completely consumed during the growth of $B_{12}P_2$. However, even though the BP matrix is not detectable, the $B_{12}P_2$ grains remain agglomerated, forming dense clusters of small crystallites.

The high concentration of grains with similar and small dimensions (<100 nm) may promote the phenomenon of coalescence. Heat-treating the BP powder at 1300 °C for 4 h has revealed $B_{12}P_2$ grains at various stages of coalescence / exaggerated growth. The grains shown in Fig. 9a exhibit a spherical shape and are interconnected by bridges, indicative of the coalescence phenomenon. As these grains grow larger, exaggerated growth can occur, leading to the formation of even larger grains, as seen in Fig. 9b, where they reach approximately 500 nm. Initially, $B_{12}P_2$ crystallites start at around 30 nm and grow to about 500 nm. During this step of coalescence / exaggerated growth, the crystallites tend to transition from a spherical to a more elongated shape, and align along preferred crystallographic directions, as illustrated Fig. 9b.

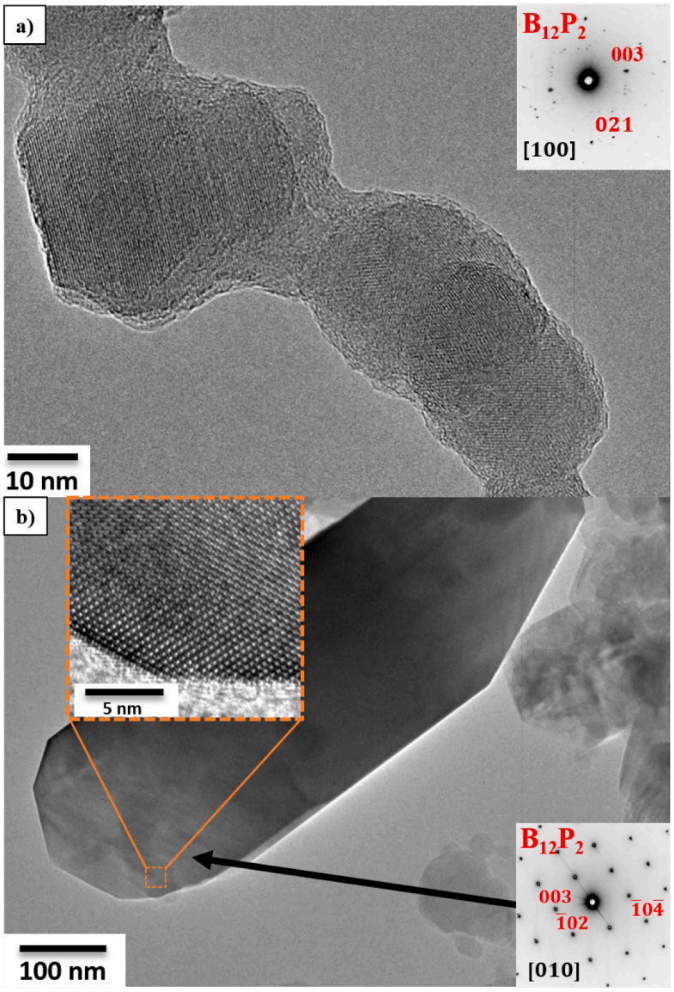

Fig. 9. TEM images and SAED patterns showing coalescence and exaggerated growth of $B_{12}P_2$ grains: (a) $B_{12}P_2$ crystallites formed after 4 h at 1300 °C; and (b) a well-crystallized $B_{12}P_2$ single crystal obtained after 4 h at 1300 °C.

4. Discussion

4.1. Phosphorus-based gas phase

According to previous studies, BP undergoes thermal decomposition into $B_{12}P_2$ at around 1150 °C under inert atmosphere [1]. In the present study, from TGA experiments, the temperature of thermal decomposition was determined close to 1120 °C. At this temperature, the appearance of cavities at the surface of BP particles can be related to the first stages of its thermal decomposition. Fig. 3 does not show any topotactic transition between BP and $B_{12}P_2$. Consequently, it is likely that the decomposition of BP phases is a gas-assisted mechanism. From a stoichiometric point of view there is a phosphorus deficiency between BP and $B_{12}P_2$. This deficiency during thermal decomposition could be due to the release of an allotropic form of phosphorus. Phosphorus exists in various allotropic forms, all of which melt to produce a liquid phase of tetraphosphorus ($P_{4(l)}$), which evaporates to a $P_{4(g)}$ gas phase at ≈ 300 °C [42]. In addition, when the temperature exceeds 825 °C, P_4 decomposes into P_2 [42–44] as follows:

$$P_{4(g)} = 2P_{2(g)} \tag{3}$$

In the thermal decomposition of BP at temperatures exceeding 825 °C, phosphorus can be released in the gas phase as $P_{4(g)}$ and/or $P_{2(g)}$, depending on the temperature. Thus, Alikhanyan et al. [22] analysed the gas phase by mass spectrometry during the decomposition of BP to $B_{12}P_2$ at a temperature of 1136 °C. Mass spectra showed the presence of ions P^+, P_2^+, P_3^+ and P_4^+along with traces of B^+, BO^+, BO_2^+ and $B_2O_2^+$. The dissociative ionisation of the P_4 molecules was found to be responsible for the intensities of the mass spectra of P^+ and P_2^+. From these results, the same authors suggested that the first reactions of the decomposition involved the formation of various phosphorus-based gaseous phases such as $P_{(g)}$, $P_{2(g)}$ and $P_{4(g)}$. The corresponding reactions (Eqs (4), (5) and (6)) are reported below:

$$\frac{6}{5}BP = \frac{1}{10}B_{12}P_2 + P_{(g)} \tag{4}$$

$$\frac{12}{5}BP = \frac{1}{5}B_{12}P_2 + P_{2(g)} \tag{5}$$

$$\frac{24}{5}BP = \frac{2}{5}B_{12}P_2 + P_{4(g)} \tag{6}$$

According to Greenwood et al. [42], $P_{(g)}$ can be obtained by dissociation of $P_{2(g)}$ for temperatures higher than 1700 °C, so well above 1120 °C. Moreover, given that P_4 is unstable at high temperature and as the experiments were carried out in under vacuum, chemical equilibrium cannot be assumed. Consequently, the decomposition reaction for temperatures higher than 1120 °C could be described in terms of two successive stages, with the second stage of dissociation of the $P_{4(g)}$

molecules acting as the rate limiting reaction:

$$\begin{cases} \frac{24}{5}BP = \frac{2}{5}B_{12}P_2 + P_{4(g)} \\ P_{4(g)} \rightarrow 2P_{2(g)} \end{cases} \quad (7)$$

4.2. A decomposition mechanism proposal

In Section 3.2.2, the experimental observations showed fragmentation of BP grains starting at 1150 °C on the surface and then throughout the grain at higher temperatures. This fragmentation phenomenon and the subsequent appearance of cavities could result from the internal stresses generated by the sudden release of the phosphorus-rich gas phase (P_2 and P_4) within a highly confined granular medium. This fragmentation phenomenon could also be due to the difference in molar volume between the reactant phase (BP) and the product phase ($B_{12}P_2$). In fact, the Pilling-Bedworth ratio (PBR) [45,46], calculated from Eq5 and corresponding to the ratio of the $B_{12}P_2$ molar volume to the BP molar volume, is <1 ($PBR_{BP} \approx 0.44$), which means the $B_{12}P_2$ film will most likely to break off. Considering the phosphorus concentration gradient in the fragmented area, as previously observed in Fig. 7b, these cavities appear to be preferential sites for the formation of Frenkel defects involving phosphorus vacancies. In an environment with internal stresses and phosphorous release, a change of crystalline structure could be induced from cubic ($F\bar{4}3m$) to rhombohedral ($R\bar{3}m$), which favours the growth of $B_{12}P_2$. Thus, all $B_{12}P_2$ nuclei seem to form at the early stages of surface degradation, where the accumulation of defects leads to the rapid precipitation of the new phase homogeneously on the surface. The accumulation of $B_{12}P_2$ nuclei at the grain edges begins to form a sufficiently thick layer to initiate the growth stage which gradually moves towards the inside of the grain. Consequently, the fully fragmented grain shown in Fig. 6e likely represents an advanced stage of growth, where the BP matrix is covered by a layer of $B_{12}P_2$.

This newly formed layer, originating from the fragmented state, exhibits a certain porosity that allows for the continuous diffusion of phosphorus from the internal interface. As decomposition progresses, the internal interface gradually shifts inward the core of the BP grain. Given that fragmentation is observed across the entire surface, the growth mode is best described as anisotropic. In this scenario, illustrated in Fig. 10, only the radial component of the growth velocity is considered, with the tangential components assumed to be infinitely large. This suggests that the initial phase is rapidly covered by the new phase, with growth occurring exclusively in the radial direction.

As the growth stage concludes, or as the forming $B_{12}P_2$ grains draw closer together, a coalescence stage may ensue, resulting in the formation of larger grains. This coalescence can be followed by a crystallisation phase, likely driven by the surface or bulk diffusion of smaller grains towards larger ones. This latter is favoured for long dwell times and/or high temperatures resulting an exaggerated growth with a preferential growth direction as seen in Fig. 9b.

In brief, the main stages of the thermal decomposition could be described as follows:

i. Release of phosphorus gas phase on the surface of BP grains from 1120 °C;
ii. Fragmentation of the BP grains under the effect of the stresses correlated to both the gas release and the crystallographic change from $F\bar{4}3m$ to $R\bar{3}m$;
iii. Growth of $B_{12}P_2$ nuclei on the surface of fragmented BP grains;
iv. Nucleation/growth and coalescence of the $B_{12}P_2$ grains;
v. Exaggerated growth of single crystals according to a preferential growth direction.

4.3. Kinetical modelling of the BP thermal decomposition

4.3.1. Decomposition kinetics

The determination of decomposition kinetics from the fractional conversion of heat-treated powders involved maintaining isotherms and

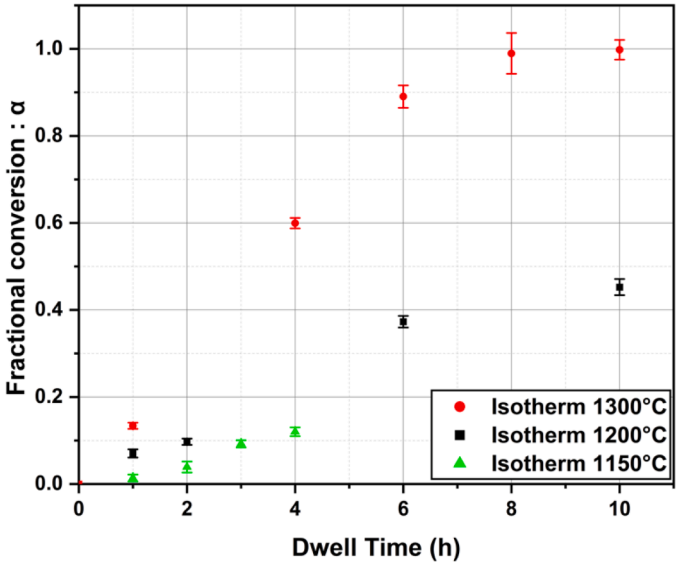

Fig. 11. Fractional conversion obtained from heat-treated powder at different isotherms. Error bars correspond to a 95 % confidence level provided from Rietveld refinement.

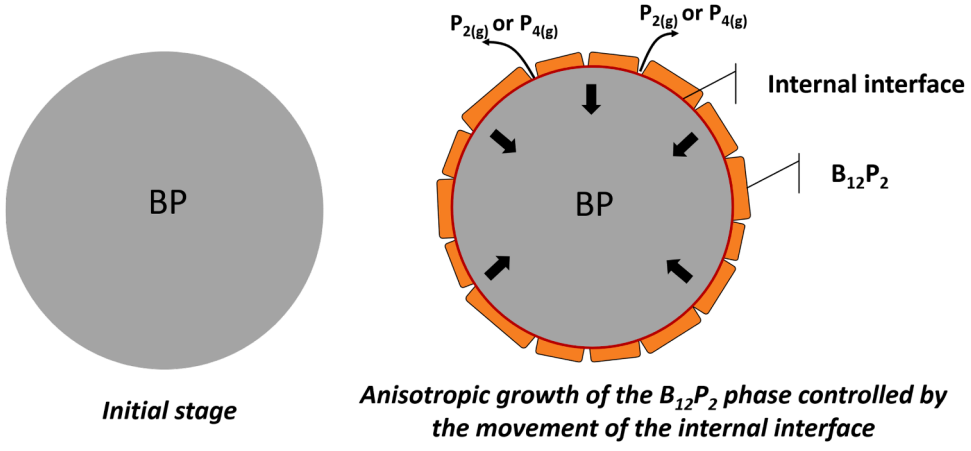

Fig. 10. Illustration of the anisotropic growth of $B_{12}P_2$.

varying the dwell time. Three isotherms were obtained at temperatures of 1150 °C, 1200 °C, and 1300 °C (Fig. 11). In the case of the 1150 °C isotherm, the temperature was too close to the decomposition temperature, limiting the decomposition kinetics. In contrast, the 1200 °C isotherm exhibited a fractional conversion of up to 0.45 with longer treatments (10 h). At the 1300 °C isotherm, a dwell time of >8 h resulted in complete decomposition.

4.3.2. Nucleation-growth modelling

A model of nucleation-growth, based on the decomposition mechanism, has been established during the present study. Assuming that the BP phase went through a phosphorous loss, it caused an abrupt modification in the crystallographic structure, leading to an increase in vacancy defects due to the departure of phosphorous atoms. The occurrence of vacancies in the crystal lattice due to this phenomenon can lead to phase instability, ultimately resulting in a phase change to $B_{12}P_2$. Simultaneously, the release of gas increases internal stresses, facilitating the rapid formation of the new phase. Consequently, in this decomposition case, it can be inferred that nucleation of the $B_{12}P_2$ phase proceeded instantly.

In this context, the thermal decomposition of BP phase can be described by a one-process model with instantaneous nucleation and slow growth [47]. To determine the appropriate kinetic model, certain assumptions can be made based on microstructural observations. Firstly, considering the thermal decomposition involved in the phase transformation, it can be assumed that the development of the phase occurred inwardly. Another assumption aims to identify the limiting reaction step during growth, which could involve diffusion, internal interface reaction, or external interface reaction. In the case of the BP thermal decomposition, the particles exhibited initially a sub-micrometric size but were fragmented into smaller, nano-sized particles. Thus, it is plausible to assume that prior to the nucleation of the $B_{12}P_2$ phase, phosphorus diffusion may have taken place when $P_{2(g)}$ was released. As a result, diffusion does not appear to be the rate-limiting step of the reaction. Instead, interfacial reactions seem to play a limiting process. Therefore, under the assumptions that a thin film of $B_{12}P_2$ rapidly formed at the surface of BP crystallites and the nucleation of the $B_{12}P_2$ phase remains homogeneous, it is reasonable to consider the growth process as anisotropic growth.

From similar assumptions (*i.e.* instantaneous nucleation, anisotropic growth), different kinetic laws have been established in the literature to describe the advancement rate as a function of the reaction time under isothermal conditions (see Table 1).

To determine the appropriate kinetic law, the fractional conversion α(t) values obtained at the 1300 °C isotherm have been compared with the theoretical expressions (Table 1). In these latter, the initial step involves the appearance of the first nuclei of the produced phase. These nuclei were identified during the initial fragmentation of BP, at a stage when the BP grains retained their original shape (Fig. 8a). Thus, the value of r_0 was fixed at 153 nm, corresponding to the average grain radius of the initial BP powder.

Considering the non-linear nature of α(t) (Fig. 11) and assuming either an external interface reaction (S_3 or S_2) or diffusion (D_3 or D_2) as the determining step, it became evident that the expressions of α(t) provided by the S_3, S_2, D_3, and D_2 laws did not align with the experimental data. Regarding R_3 and R_2, which assume an internal interface reaction as the limiting step, a Levenberg-Marquardt algorithm was applied to optimize ϕ and fit it to the experimental data (Fig. 12).

By comparing the coefficient of correlation (r^2), the R_2 law assuming cylindrical particles was found to fit better, with an r^2 equal to 0.992 compare to 0.984 for the R_3 law. This conclusion is supported by TEM observations, which indicated that during the growth of $B_{12}P_2$, the particles exhibited a preferred crystallographic orientation which can be assimilated as cylindrical (Fig. 9b). Consequently, the assumption of decomposition being governed by instantaneous nucleation and anisotropic growth appears to align with the experimental data.

The fitting model seems to validate the decomposition mechanism illustrated in Fig. 10, where the anisotropic growth of the $B_{12}P_2$ phase is controlled by the movement of the internal interface, and the particle shape can be assimilated to a cylinder. Thus, under these conditions, it is suggested that the thermal decomposition is primarily governed by the growth process of $B_{12}P_2$.

Table 1
Expression of α(t) for one-process models with instantaneous nucleation and anisotropic growth [47], ϕ: Areic reactivity of growth (mol.s^{-1}.m^{-2}); V_m: Molar volume (m^3.mol^{-1}); l_0: Constant length (m); r_0: Initial radius of a particle (m); t: Time (s).

Limiting reaction step	Spherical particle ($n = 3$)	Cylindrical particle ($n = 2$)
Internal interface (R_n)	$\alpha = 1 - \left(1 - \Phi\frac{V_m(BP)}{r_0}t\right)^3$	$\alpha = 1 - \left(1 - \Phi\frac{V_m(BP)}{r_0}t\right)^2$
External interface (S_n)	$\alpha = \Phi\frac{3V_m(BP)}{r_0}t$	$\alpha = \Phi\frac{2V_m(BP)}{r_0}t$
Diffusion (D_n)	$(1-\alpha)^{\frac{2}{3}} - \frac{2\alpha}{3} = \Phi\frac{2V_m(BP)l_0}{{r_0}^2}t$	$(1-\alpha)ln(1-\alpha) + \alpha = \Phi\frac{4V_m(BP)l_0}{{r_0}^2}t$

5. Conclusions

This study focused on investigating the thermal decomposition of BP into $B_{12}P_2$, with a specific emphasis on the heterogenous solid-gas process using BP powder synthesized via SHS. The combination of structural and microstructural analysis techniques has provided relevant insights into the transformation mechanism of the BP phase into $B_{12}P_2$. It was shown that thermal decomposition of the BP phase starts at 1120 °C. Beyond this critical temperature, several thermal treatments were applied to the powder, revealing the fragmentation of BP grains into smaller particles, accompanied by the release of phosphorous gases ($P_{2(g)}$, $P_{4(g)}$). A proposed decomposition mechanism described the phase transition from cubic BP to rhombohedral $B_{12}P_2$. The process begins with the fragmentation of BP grains caused by gas release and an environment with internal stresses, which leads to phase instability due to gaseous phosphorus release. This in turn leads to nucleation and coalescence/anisotropic growth of the $B_{12}P_2$ phase.

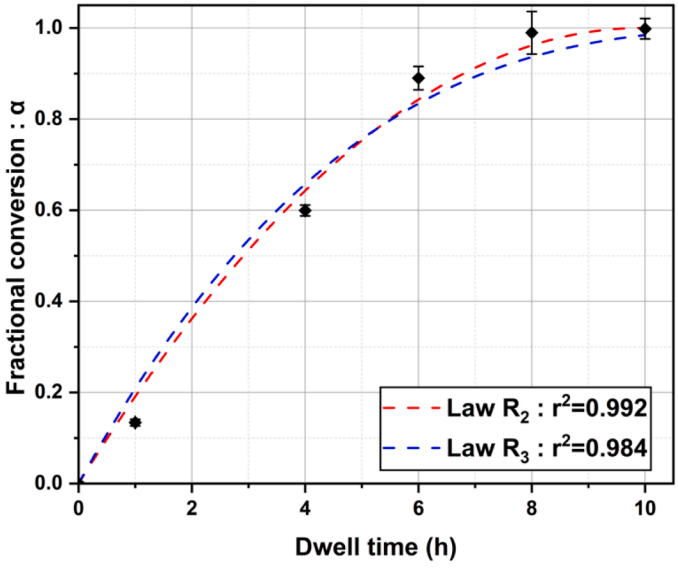

Fig. 12. Fractional conversion obtained from heat-treated powder at 1300 °C for various dwell times. The R_2 and R_3 laws were fitted using the Levenberg-Marquardt algorithm, with r^2 representing the coefficient of correlation.

Furthermore, employing Rietveld refinements on thermally treated powder allowed for the determination of fractional conversions across different isotherms. Notably, an isotherm at 1300 °C described the fractional conversion rate. The analysis of experimental data led to the investigation of a one-process nucleation-growth model, featuring instantaneous nucleation and anisotropic growth. One model (R_2) emerged as the most promising, displaying a suitable coefficient of correlation.

CRediT authorship contribution statement

Yves Tahan: Writing – original draft, Methodology, Investigation. **Olivier Rapaud:** Writing – review & editing, Supervision, Methodology. **Nicolas Pradeilles:** Writing – review & editing, Supervision, Methodology. **Pierre Carles:** Investigation, Funding acquisition. **Alexandre Maître:** Writing – review & editing, Supervision. **Sarah Dine:** Methodology, Investigation, Funding acquisition. **Dominique Vrel:** Investigation, Funding acquisition. **Hicham Moutaabbid:** Writing – review & editing, Methodology. **Yann Le Godec:** Writing – review & editing, Methodology. **Cécile Genevois:** Investigation, Methodology, Writing – review & editing. **Mathieu Allix:** Investigation, Methodology.

Declaration of interests

The authors declare that they have no known competing financial interests or personal relationships that could have appeared to influence the work reported in this paper.

Acknowledgements

The authors would like to thank AID (Defence Innovation Agency) for funding. This work was also supported by institutional grant from the National Research Agency with the reference ANR-20-ASTR-0020. The project benefitted from the microscopy facilities of the MACLE-CVL Platform which was co-funded by the European Union and Centre-Val de Loire Region (FEDER).

Supplementary materials

Supplementary material associated with this article can be found, in the online version, at doi:10.1016/j.actamat.2024.120495.

References

[1] R. Gui, Z. Xue, X. Zhou, C. Gu, X. Ren, H. Cheng, D. Ma, J. Qin, Y. Liang, X. Yan, J. Zhang, X. Zhang, X. Yu, L. Wang, Y. Zhao, S. Wang, Strain stiffening, high load-invariant hardness, and electronic anomalies of boron phosphide under pressure, Phys. Rev. B 101 (2020) 035302, https://doi.org/10.1103/PhysRevB.101.035302.
[2] R.J. Archer, R.Y. Koyama, E.E. Loebner, R.C. Lucas, Optical absorption, electroluminescence, and the band gap of BP, Phys. Rev. Lett. 12 (1964) 538–540, https://doi.org/10.1103/PhysRevLett.12.538.
[3] J.I. Ejembi, I.H. Nwigboji, L. Franklin, Y. Malozovsky, G.L. Zhao, D. Bagayoko, Ab-initio calculations of electronic, transport, and structural properties of boron phosphide, J. Appl. Phys. 116 (2014) 103711, https://doi.org/10.1063/1.4894692.
[4] K. Woo, K. Lee, K. Kovnir, BP: synthesis and properties of boron phosphide, Mater. Res. Express 3 (2016) 074003, https://doi.org/10.1088/2053-1591/3/7/074003.
[5] G.A. Slack, T.F. McNelly, E.A. Taft, Melt growth and properties of B6P crystals, J. Phys. Chem. Solids 44 (1983) 1009–1013, https://doi.org/10.1016/0022-3697(83)90151-8.
[6] Y. Kumashiro, T. Mitsuhashi, S. Okaya, F. Muta, T. Koshiro, Y. Takahashi, M. Mirabayashi, Thermal conductivity of a boron phosphide single-crystal wafer up to high temperature, J. Appl. Phys. 65 (1989) 2147–2148, https://doi.org/10.1063/1.342867.
[7] Y. Kumashiro, T. Yokoyama, K. Sato, Y. Ando, S. Nagatani, K. Kajiyama, Electrical and thermal properties of B12P2 Wafers, J. Solid State Chem. 154 (2000) 33–38, https://doi.org/10.1006/jssc.2000.8807.
[8] J.S. Kang, H. Wu, Y. Hu, Thermal properties and phonon spectral characterization of synthetic boron phosphide for high thermal conductivity applications, Nano Lett 17 (2017) 7507–7514, https://doi.org/10.1021/acs.nanolett.7b03437.
[9] Q. Zheng, S. Li, C. Li, Y. Lv, X. Liu, P.Y. Huang, D.A. Broido, B. Lv, D.G. Cahill, High thermal conductivity in isotopically enriched cubic boron phosphide, Adv. Funct. Mater. 28 (2018) 1805116, https://doi.org/10.1002/adfm.201805116.
[10] V.L. Solozhenko, V. Bushlya, Mechanical properties of boron phosphides, J. Superhard Mater. 41 (2019) 84–89, https://doi.org/10.3103/S1063457619020023.
[11] B. Stone, D. Hill, Semiconducting properties of cubic boron phosphide, Phys. Rev. Lett. 4 (1960) 282–284, https://doi.org/10.1103/PhysRevLett.4.282.
[12] G.I. Post. Semiconducting Materials: Part 2 An Investigation of the Boron-Phosphorous System, New York State College of Ceramics at Alfred University, 1965.
[13] V.A. Mukhanov, P.S. Sokolov, O. Brinza, D. Vrel, V.L. Solozhenko, Self-propagating high-temperature synthesis of boron subphosphide B12P2, J. Superhard Mater. 36 (2014) 18–22, https://doi.org/10.3103/S1063457614010031.
[14] V.A. Mukhanov, O.O. Kurakevych, V.L. Solozhenko, Thermodynamic model of hardness: particular case of boron-rich solids, J. Superhard Mater. 32 (2010) 167–176, https://doi.org/10.3103/S1063457610030032.
[15] H.R. Jiang, W. Shyy, M. Liu, L. Wei, M.C. Wu, T.S. Zhao, Boron phosphide monolayer as a potential anode material for alkali metal-based batteries, J. Mater. Chem. A 5 (2017) 672–679, https://doi.org/10.1039/C6TA09264K.
[16] T. Udagawa, T. Yamashita, Boron phosphide-based semiconductor device production method thereof light-emitting diode and boron phosphide-based semiconductor layer, US20050121693A1, 2005.
[17] W. Liang, L. Zhang, X. Xiang, J. Wang, L. Zhang, B. Wu, Y. Wang, Y. Zeng, S. Guan, Q. Tang, F. Peng, Growth of millimeter-size single-crystal boron phosphide by eutectic melt at 5.0 GPa and 3000 °C, Solid State Commun 327 (2021) 114206, https://doi.org/10.1016/j.ssc.2021.114206.
[18] V.L. Solozhenko, V.A. Mukhanov, P.S. Sokolov, Y.Le Godec, K.A. Cherednichenko, Z. Konôpková, Melting of B12P2 boron subphosphide under pressure, High Press. Res 36 (2016) 91–96, https://doi.org/10.1080/08957959.2016.1142542.
[19] V.L. Solozhenko, V.A. Mukhanov, On melting of boron phosphide under pressure, J. Superhard Mater. 37 (2015) 438–439, https://doi.org/10.3103/S1063457615060106.
[20] J.L. Peret, Preparation and properties of the boron phosphides, J. Am. Ceram. Soc. 47 (1964) 44–46, https://doi.org/10.1111/j.1151-2916.1964.tb14639.x.
[21] F.V. Williams, R.A. Ruehrwein, The preparation and properties of boron phosphides and arsenides1, J. Am. Chem. Soc. 82 (1960) 1330–1332, https://doi.org/10.1021/ja01491a014.
[22] A.S. Alikhanyan, A.V. Steblevskii, Y.K. Grinberg, V.I. Gorgoraki, Mass-spectrometric investigation of the vaporisation of boron phosphide, Russ. J. Phys. Chem. 49 (1975) 1846–1848.
[23] V.I. Matkovich, Unit cell, space group and composition of a lower boron phosphide, Acta Crystallogr 14 (1961) 93, https://doi.org/10.1107/S0365110x61000425.
[24] C.E. Myers, Heat of dissociation of boron phosphide, BP(s), J. Phys. Chem. 65 (1961) 2111–2112, https://doi.org/10.1021/j100828a510.
[25] V.-A. Ha, B. Karasulu, R. Maezono, G. Brunin, J.B. Varley, G.-M. Rignanese, B. Monserrat, G. Hautier, Boron phosphide as a p-type transparent conductor: optical absorption and transport through electron-phonon coupling, Phys. Rev. Mater. 4 (2020) 065401, https://doi.org/10.1103/PhysRevMaterials.4.065401.
[26] L. Shi, P. Li, W. Zhou, T. Wang, K. Chang, H. Zhang, T. Kako, G. Liu, J. Ye, n-type boron phosphide as a highly stable, metal-free, visible-light-active photocatalyst for hydrogen evolution, Nano Energy 28 (2016) 158–163, https://doi.org/10.1016/j.nanoen.2016.08.041.
[27] A. Crovetto, J.M. Adamczyk, R.R. Schnepf, C.L. Perkins, H. Hempel, S.R. Bauers, E. S. Toberer, A.C. Tamboli, T. Unold, A. Zakutayev, Boron phosphide films by reactive sputtering: searching for a p-type transparent conductor, Adv. Mater. Interfaces 9 (2022) 2200031, https://doi.org/10.1002/admi.202200031.
[28] J.B. Varley, A. Miglio, V.-A. Ha, M.J. van Setten, G.-M. Rignanese, G. Hautier, High-throughput design of non-oxide p-type transparent conducting materials: data mining, search strategy, and identification of boron phosphide, Chem. Mater. 29 (2017) 2568–2573, https://doi.org/10.1021/acs.chemmater.6b04663.
[29] Y. Kumashiro, T. Yokoyama, J. Nakamura, K. Matsuda, H. Yoshida, J. Takahashi, Thermoelectric properties of boron and boron phosphide film, MRS Online Proc. Libr. 242 (1992) 629–635, https://doi.org/10.1557/PROC-242-629.
[30] V.A. Mukhanov, P.S. Sokolov, Y.L. Godec, V.L. Solozhenko, Self-propagating high-temperature synthesis of boron phosphide, J. Superhard Mater. 35 (2013) 415–417, https://doi.org/10.3103/S1063457613060105.
[31] Y.L. Godec, V.A. Mukhanov, V.L. Solozhenko, P.S. Sokolov, Production of boron phosphide by reduction of boron phosphate with an alkaline metal, WO2015097244A1, 2015.
[32] Y.L. Godec, V.A. Mukhanov, V.L. Solozhenko, P.S. Sokolov, D. Vrel, Mechanochemical process for the production of BP, B12P2 and mixtures thereof, in particular as nanopowders, US10519039B2, 2019.
[33] V.A. Mukhanov, D. Vrel, P.S. Sokolov, Y.L. Godec, V.L. Solozhenko, Ultra-fast mechanochemical synthesis of boron phosphides, BP and B12P2, Dalton Trans 45 (2016) 10122–10126, https://doi.org/10.1039/C6DT00435K.
[34] J.A. Perri, S.La Placa, B. Post, New group III-group V compounds: BP and BAs, Acta Crystallogr 11 (1958) 310, https://doi.org/10.1107/S0365110x58000827.
[35] P. Yang, T.L. Aselage, Synthesis and cell refinement for icosahedral boron phosphide B12P2, Powder Diffr 10 (1995) 263–265, https://doi.org/10.1017/S0885715600014949.
[36] H. Moissan, Étude des phosphoiodures de bore, C. R. Acad. Sci. 113 (1891) 624–627.
[37] H. Moissan, Préparation et propriétés des phosphures de bore, C. R. Acad. Sci. 113 (1891) 726–729.

[38] A. Besson, Combinaison du bromure de bore avec l'hydrogène phosphoré. Phosphure de bore, C. R. Acad. Sci. 113 (1891) 78–80.
[39] A. Besson, Sur les phosphures de bore, C. R. Acad. Sci. 113 (1891) 772–773.
[40] E.M. Kelder, P.J. van der Put, J. Schoonman, Thermochemical data of boron subphosphide, Thermochim. Acta 306 (1997) 105–108, https://doi.org/10.1016/S0040-6031(97)00308-0.
[41] R. Klement, SECTION 9 - Phosphorus, in: G. Brauer (Ed.), Handb. Prep. Inorg. Chem, 2nd Ed, Academic Press, 1963, pp. 518–590, https://doi.org/10.1016/B978-0-12-395590-6.50017-X.
[42] 12 - Phosphorus, in: N.N. Greenwood, A. Earnshaw (Eds.), Chem. Elem, 2nd Ed, Butterworth-Heinemann, Oxford, 1997, pp. 473–546, https://doi.org/10.1016/B978-0-7506-3365-9.50018-3.
[43] H. Bock, H. Mueller, Gas-phase reactions. 44. The phosphorus P4 .dblarw. 2P2 equilibrium visualized, Inorg. Chem. 23 (1984) 4365–4368, https://doi.org/10.1021/ic00193a051.
[44] N.A. Piro, J.S. Figueroa, J.T. McKellar, C.C. Cummins, Triple-bond reactivity of diphosphorus molecules, Science 313 (2006) 1276–1279, https://doi.org/10.1126/science.1129630.
[45] N.B. Pilling, R.E. Bedworth, Oxidation of copper-nickel alloys at high temperatures, Ind. Eng. Chem. 17 (1925) 372–376, https://doi.org/10.1021/ie50184a013.
[46] C. Xu, W. Gao, Pilling-Bedworth ratio for oxidation of alloys, Mater. Res. Innov. 3 (2000) 231–235, https://doi.org/10.1007/s100190050008.
[47] M. Soustelle, Laws of evolutions in the one-process models with instantaneous nucleation and anisotropic growth. Handb. Heterog. Kinet., John Wiley & Sons, Ltd, 2013, pp. 849–852, https://doi.org/10.1002/9781118557730.app3.